Analysis of shipboard aerosol optical thickness measurements from multiple sunphotometers aboard the R/V Ronald H. Brown during the Aerosol Characterization Experiment—Asia

Mark A. Miller, Kirk Knobelspiesse, Robert Frouin, Mary Jane Bartholomew, R. Michael Reynolds, Christophe Pietras, Giulietta Fargion, Patricia Quinn, and François Thieuleux

Marine sunphotometer measurements collected aboard the R/V Ronald H. Brown during the Aerosol Characterization Experiment—Asia (ACE-Asia) are used to evaluate the ability of complementary instrumentation to obtain the best possible estimates of aerosol optical thickness and Ångstrom exponent from ships at sea. A wide range of aerosol conditions, including clean maritime conditions and highly polluted coastal environments, were encountered during the ACE-Asia cruise. The results of this study suggest that shipboard hand-held sunphotometers and fast-rotating shadow-band radiometers (FRSRs) yield similar measurements and uncertainties if proper measurement protocols are used and if the instruments are properly calibrated. The automated FRSR has significantly better temporal resolution (2 min) than the hand-held sunphotometers when standard measurement protocols are used, so it more faithfully represents the variability of the local aerosol structure in polluted regions. Conversely, results suggest that the hand-held sunphotometers may perform better in clean, maritime air masses for unknown reasons. Results also show that the statistical distribution of the Ångstrom exponent measurements is different when the distributions from hand-held sunphotometers are compared with those from the FRSR and that the differences may arise from a combination of factors.

OCIS codes: 010.0010, 120.0120, 280.0280, 290.0290.

1. Introduction

The radiation transfer properties of tropospheric aerosols are one of the largest sources of uncertainty in climate models.[1] The uncertainty is particularly acute over the world's oceans because there is a lack of *in situ* measurements of aerosol radiation transfer characteristics and associated chemical properties. *In situ* measurements are also required for evaluation of satellite estimates of the spatial distribution and radiation-transfer characteristics of the aerosols in the marine atmosphere.[2–7] The need for accurate surveys of marine aerosol properties during the past decade has stimulated rapid progress in overocean sunphotometry, which is the subject of this paper.

Sunphotometers measure narrowband irradiance from which two fundamental quantities can be derived that describe the attenuating characteristics of the turbid atmosphere: aerosol optical thickness τ_λ and the Ångström exponent,[8] α. The former is a coefficient that describes the reduction in the direct-normal irradiance in a channel centered on wavelength λ, and the latter quantifies the wavelength dependence of τ_λ. The Ångström exponent[8] used here is a single-parameter version of the original two-parameter formulation.[9] Although Ångström vehemently argues that a two-parameter formulation is

M. A. Miller (miller@bnl.gov), M. J. Bartholomew, and R. Michael Reynolds are with the Earth System Science Division, Building 490D, Brookhaven National Laboratory, Upton, New York 11973. K. Knobelspiesse, C. Pietras, and G. Fargion are with Science Systems and Applications, Inc., NASA SIMBIOS Project, Goddard Space Flight Center, Greenbelt, Maryland 20771. R. Frouin is with the Scripps Institution of Oceanography, University of California, San Diego, La Jolla, California 92093. P. Quinn is with the Pacific Marine Environmental Laboratory, Seattle, Washington 98115. F. Thieuleux is with the Laboratoire d'Optique Atmosphérerique, Université des Sciences et Technologies de Lille, Villeneuve d'Ascq, France.

Received 11 May 2004; accepted 29 July 2004.
0003-6935/05/183805-16$15.00/0

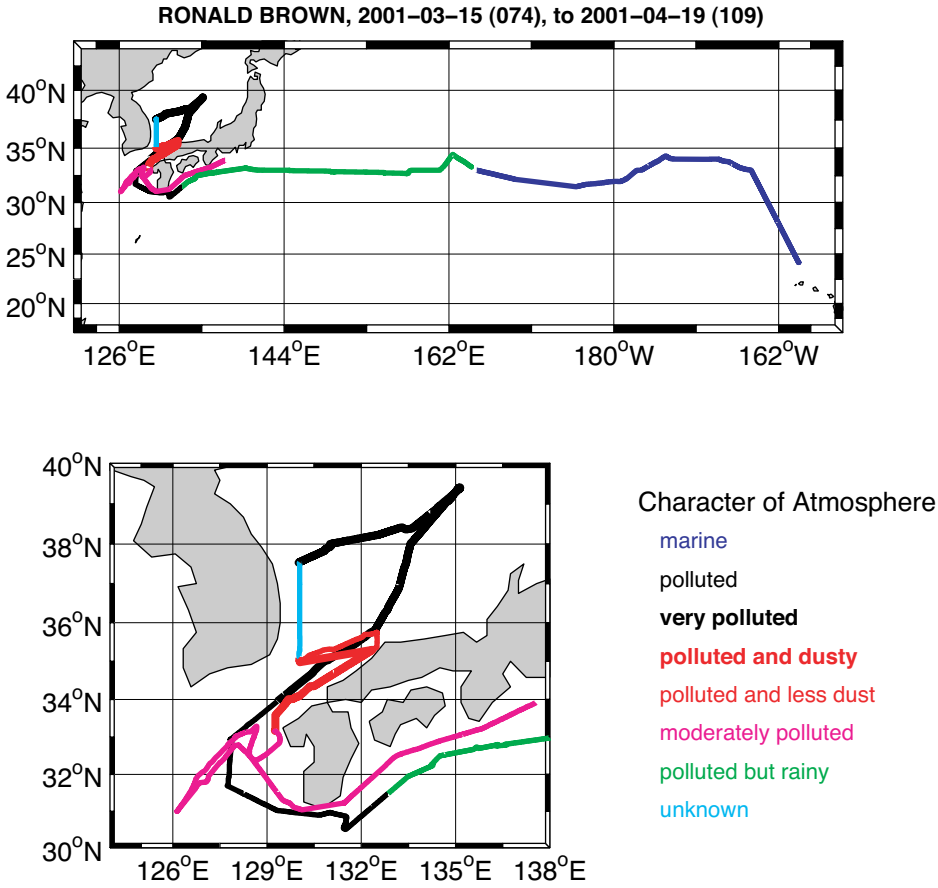

Fig. 1. Cruise trajectory of the R/V Ronald H. Brown during the ACE-Asia cruise. Latitudes and longitudes are indicated, and the cruise trajectory is color coded according to the type of aerosol suggested by a trajectory analysis. The types of aerosol present are given in the accompanying legend. (a) The complete cruise trajectory, (b) a close-up of the cruise trajectory in the vicinity of Japan.

necessary to represent observed complexity, it can be shown that the wavelength-dependent parameter in his two-parameter model is the dominant parameter. Therefore we have chosen a single-parameter formulation because it adequately represents the observations analyzed here and provides the simplest means to present the data.

It is difficult to operate sunphotometers at sea because they are sensitive to platform motion. Nonetheless, substantial progress has been made and new instruments and techniques have emerged. These include simple, commercially available hand-held devices (the Microtops ozone monitor and sunphotometer,[10,11] more-sophisticated, research-grade hand-held devices,[12] and marine fast-rotating shadow-band radiometers[13,14] (FRSRs). All these sunphotometers are passive and measure the narrowband τ_λ in 10-nm-wide channels scattered across the visible–near-infrared spectrum. Additionally, the FRSRs decompose the irradiance field into direct-normal and diffuse components, which can be used to retrieve additional information about the nature of the aerosol.

Our purpose in this paper is to compare and evaluate the sunphotometers that are being used to measure τ_λ and α from ships at sea and to provide guidance for the handling, processing, and interpretation of these data. Sunphotometers and other instruments deployed aboard the R/V Ronald H. Brown during the Aerosol Characterization Experiment—Asia (ACE-Asia), which was conducted in the vicinity of eastern Asia, are analyzed. An estimate of the time series of τ_λ and α for the cruise period is computed by use of an unweighted average of data from all the instruments used aboard the ship. Previous measurements of the aerosol optical thickness time series from the R/V Ronald H. Brown during the ACE-Asia have been published,[15] but they were collected with a single commercial hand-held sunphotometer. The measurements presented here originate from multiple independent platforms and have undergone strict quality control and a dutiful, uncertainty analysis. These ACE-Asia data demonstrate a wide range of issues related to the use of over-ocean radiation and aerosol measurements and provide an excellent medium for instrument and technique evaluation.

2. Data Set

The R/V Ronald H. Brown left Hawaii on 15 March 2001 and traveled across the North Pacific Ocean at approximately 30–35 N latitude [Fig. 1(a)]. The ship

Table 1. Sunphotometers Deployed on the R/V Ronald H. Brown during ACE-Asia

Instrument	Center Wavelengths per Band (nm), All Columns											
Simbad #03[a]				443	490		560		670		870	
SimbadA #02[a]	350	380	412	443	490	510	560	620	670	750	870	
Microtops #3773[b]				440	500				675		870	936
Microtops #4080		380		440	500				675		870	
FRSR[c]			410		500			615	680		870	940

[a]Uncertainties for the Simbad and Simbada aerosol optical thickness values are estimated to be 0.012–0.019.[11]

[b]SIMBIOS project sunphotometers are calibrated on land by a cross calibration to Cimel sunphotometers maintained by the AERONET project.[20] The Cimel sunphotometers are calibrated by the Langley method at Mauna Loa. The uncertainty for the Microtops aerosol optical thickness values made at sea is 0.025.[10,11]

[c]Calibration of this instrument is tied to satellite-measured extraterrestrial irradiance.[14] The uncertainty of the aerosol optical thickness values determined by the FRSR is 0.03.[14]

subsequently passed into the Philippine Sea, near the southern tip of Japan, through the northern part of the East China Sea, and into the Sea of Japan, where it followed a complex trajectory [Fig. 1(b)]. During periods when cloud conditions permitted, measurements of τ_λ and α were collected with two Microtops sunphotometers, one Simbad and one advanced Simbad (SimbadA) radiometer, and a FRSR, which are described below. We used a total sky imager (TSI) to obtain a visual assessment of the sky condition at the time of the measurement. Based on backtrajectories,[16] seven relatively distinct aerosol regimes were encountered: marine, polluted, heavily polluted, polluted and dusty, polluted and less dusty, moderately polluted, and polluted but rainy [Figs. 1(a) and 1(b)]. Aerosol characterization on the basis of backtrajectories was not possible for a small portion of the cruise trajectory. As the plot shows, generally polluted and dusty conditions were encountered in the vicinity of Japan, particularly in the Sea of Japan.

A. Sunphotometers

Each sunphotometer used on the R/V Ronald H. Brown during the ACE-Asia arrives at an estimate of the direct-normal irradiance by using a slightly different method, but all use the Langley technique to determine the extraterrestrial irradiance that is used to compute τ_λ. The Simbad, SimbadA, and Microtops are collimated radiometers with several narrow passbands that are manually pointed toward the Sun to measure the direct-normal component of solar irradiance. The FRSR determines the direct-normal irradiance by subtracting an estimate of the diffuse irradiance made by occulting the solar disk with a mechanical arm from a measurement of the total hemispheric irradiance.[13,14] An adjustment is made to account for the portion of the diffuse component inadvertently occulted by the arm during the diffuse measurement. A summary of the instruments used in this study is given in Table 1.

The application of sunphotometry on a ship has the special problem of ship motion. The ship has a periodic rocking motion with a typical period of 5–15 s and a mean tilt, which can be related to weight distribution, wind forcing, and the directional wave field. It will change slowly over hours or days, or more suddenly if the ship makes an abrupt direction change. Rocking is typically $\pm 1°$–$5°$ on the R/V Ronald H. Brown, whereas the mean tilt can be $\pm 1°$–$2°$. Each radiometric technique used to measure τ_λ and α on the ship during the ACE-Asia accommodates ship motion in a different manner. The operator mechanically stabilizes the hand-held devices, and the FRSR compensates for ship motion by measuring platform motion and compensating for it in postprocessing.

1. *Hand-Held Instruments*

Two Microtops hand-held sunphotometers were used aboard the R/V Ronald H. Brown during the ACE-Asia. They were manufactured by Solar Light, Inc., and operated by representatives from the NASA Sensor Intercomparison and Merger for Biological Oceanographic Studies (SIMBIOS) and the National Oceanic and Atmospheric Administration's Pacific Marine Environmental Laboratory (NOAA-PMEL), respectively. Complementing these instruments were two research-grade hand-held sunphotometers (Simbad and SimbadA) designed by the Laboratorie d'Optique Atmospherique of the University of Lille, France. Measurements are taken when the observer deems the sky to be clear of clouds, and photons captured by a collimator through a lens fall upon photodiode detectors, which produce an electrical current proportional to the radiant energy. There is a visual targeting mechanism to enable the user to aim the collimator manually in the direction of the solar disk. For the Simbad, SimbadA, and Microtops instruments several measurements over a period of seconds are collected to form a measurement. Uncertainties for the Simbad and Simbada hand-held units[12] are estimated in the published literature to be 0.012–0.019, and uncertainties for the Microtops units are thought to be similar.[10,11]

An important issue, especially in marine conditions, is the sampling strategy. The normal measurement sensitivity to the dexterity of the user is compounded by ship motion, thereby influencing measurement accuracy through sun-pointing errors.[10] Sun-pointing errors bias the measurements toward higher values of $\tau_{\lambda A}$. Early deployments of Microtops units on ships used the manufacturer-supplied measurement protocol to determine $\tau_{\lambda A}$, but

Table 2. Calibration Information for Hand-Held Radiometers Used in This Study

Photometer SN	Date	Calibration Technique	Site	Principal Investigator's Name
Microtops #3773	20 September 2000	Cross calibration	NASA/Goddard	J. Welton/K. Knobelspiesse
	06 July 2001	Cross calibration	NASA/Goddard	
Microtops #4080	Earlier cruise	Langley–Bouguer	Mauna Loa	P. Quinn
	Five months later	Langley–Bouguer	Mauna Loa	
Simbad #03	30 December 2000	Langley–Bouguer	Stephenson Peak[a]	R. Frouin
	28 June 2001	Langley–Bouguer	Stephenson Peak	
SimbadA #02	8 March 2001	Langley–Bouguer	Stephenson Peak	P.-Y. Deschamps
	1 May 2001	Langley–Bouguer	Stephenson Peak	

[a]Located in the Laguna Mountains, ~100 km east of San Diego, altitude 1896 m, latitude 32.9, longitude −116.3.

later studies showed that this default protocol could introduce significant uncertainty on a moving platform. The SIMBIOS Microtops uses a specially designed protocol and postprocessing algorithm to remove this effect.[17] The SIMBIOS Microtops measurement protocol is to collect 20 samples over a 6-s period and store the sample with the largest voltage, which is used to compute $\tau_{\lambda A}$. After the experiment, a postprocessing algorithm is used to further screen measurements to remove sun-pointing errors. The data are naturally grouped into discrete segments that correspond to a period of several minutes. For each sample period, one computes a coefficient of variation (CoV) by dividing the standard deviation of the measurement set by its mean. If the CoV is above a threshold of 0.05, the highest value of $\tau_{\lambda A}$ is removed and the CoV recomputed. This iteration continues until the CoV is less than the threshold or there are not enough points with which to compute the standard deviation. Data are accepted only if the iteration is successful in all measurement bands.

The SIMBIOS protocol was used for one Microtops device during the ACE-Asia, although the manufacturer-supplied protocol was supposed to be used for the PMEL Microtops. The manufacturer-supplied default protocol is to average the 4 lowest $\tau_{\lambda A}$ samples of a set of 32. Unfortunately, the PMEL Microtops unit was mistakenly set to average the lowest 20 measurements of the 32, which appreciably increased measurement uncertainty. A postprocessing algorithm was employed to make the PMEL Microtops data consistent with the SIMBIOS protocol. Measurements whose standard deviation in the 20 averaged samples exceeded the published uncertainty of the SIMBIOS protocol[18] (0.015) were removed. Therefore, relatively few measurements from the PMEL Microtops were available for analysis.

The Simbad and SimbadA protocol is conceptually similar to the Microtops manufacturer-supplied protocol but with a higher sampling rate that makes them less sensitive to platform motion. Each series of Simbad and SimbadA $\tau_{\lambda A}$ are collected during a 10-s period at 10-Hz frequency, so 100 samples are collected during the measurement period. One averages the lowest sample values of $\tau_{\lambda A}$ to determine $\tau_{\lambda A}$ for the 10-s measurement period. The higher sampling frequency of the Simbad and SimbadA radiometers increases the probability that samples will be collected exclusively along the direct-normal solar vector.

The hand-held sunphotometers were calibrated before and after the ACE-Asia experiment. Two calibration methods were used: the Langley technique and a calibration transfer procedure (Table 2). The Langley technique measure's direct-normal irradiance in clear skies at various solar zenith angles and extrapolate in log space to predict the magnitude of the signal at the top of the atmosphere. The Langley technique requires exceptionally clear conditions such as those encountered at sites such as the high-altitude observatory at Mauna Loa, Hawaii. The calibration transfer method uses concurrent measurements from an uncalibrated sunphotometer and adjusts them to be consistent with a calibrated instrument. Reference instruments used by the SIMBIOS project are sunphotometers calibrated at Mauna Loa every three months.

2. *Marine Fast-Rotating Shadow-Band Radiometer*

The marine FRSR used on the R/V Ronald H. Brown used a seven-channel (one broadband, six 10-nm narrowband) silicon-detector-based optical head and a semicircular occulting arm.[13] The FRSR was placed aboard the ship approximately two months before the beginning of the ACE-Asia campaign. The occulting arm circumscribes a complete rotation centered on the optical head, thereby occulting a band of the sky, with a revisitation period of 6.5 s. The signals from all seven optical channels are sampled rapidly, so the shadow cast by the shadow band onto the detectors can be recognized and recorded. Ship motion is compensated for mathematically through careful accounting of platform position.

We used the Langley technique to calibrate the FRSR before and after the ACE-Asia because a calibration could not be used at sea owing to uncertainty in the platform orientation.[13] Langley calibrations of FRSRs on land generally provide values of the extraterrestrial irradiance that agree within 1–2% of a specific published solar spectrum.[14] We derived the extraterrestrial irradiances to process FRSR data for the ACE-Asia campaign by convolving the instrument's bandpass with a specific extraterrestrial solar

spectral irradiance, rather than through frequent Langley analyses as would be the case on land. Because the FRSR is deployed for extended periods, the instrument's gain is continuously monitored by comparison of the broadband channel with more-stable broadband measurements from a coincident Eppley pyranometer mounted upon the FRSR platform. Instrument gains are adjusted in postprocessing in an attempt to maintain a calibration consistent with the specified reference extraterrestrial irradiance, though the data can always be adjusted to be consistent with other published extraterrestrial irradiances.[19] Whereas this broadband adjustment technique is known to be slightly sensitive to the column-integrated water vapor, drifts in the instrument gain are easily identified because their signal does not fluctuate like that of the integrated water vapor.

The FRSR differs from hand-held sunphotometers because it collects data continuously. Because the marine boundary layer is a particularly cloudy environment, measurements of $\tau_{\lambda A}$ are often contaminated by $\tau_{\lambda C}$, the optical thickness of clouds. In hand-held sunphotometers, the operator filters clouds by taking observations at times when the Sun's disk is completely visible. The FRSR collects data continuously, which dictates that cloud contamination will naturally be included in the data record because there is no initial subjective filtering. Therefore an automatic cloud-filtering algorithm is required.

The conceptual foundation of the FRSR cloud filter is the different levels of variability observed in the two signals, $\tau_{\lambda A} + \tau_{\lambda C}$ and $\tau_{\lambda A}$. Broken cloud fields show large variations in τ_λ as clouds drift across the solar disk. In contrast, $\tau_{\lambda A}$ is reasonably constant over periods of an hour or two owing to the time scales of the physical processes that modulate changes in the aerosol load. The filter is applied to a window that comprises $n = 11$ consecutive values of $\tau(t)$, or equivalently $\tau(i)$, where i is an incremental integer index. Symbolically, the window is defined as $\tau(t[i - 5]) \rightarrow \tau(t[i + 5])$ and $\tau(i)$ is considered cloud free if these three conditions are satisfied:

$$\begin{aligned} 2.0 \geq \tau(i) \geq 0.005 \\ \oplus \ |t(i-5) - t(i+5)| < 2 \text{ hours} \\ \oplus \ \mu_\tau^{\text{window}} < 0.05 < |\tau(i) - \mu_\tau^{\text{window}}|. \end{aligned} \quad (1)$$

In relation (1), $\sigma_\tau^{\text{window}}$ and $\sigma_\tau^{\text{window}}$ are the arithmetic mean and the standard deviation of the windowed data, respectively, and $\oplus$ signifies a logical AND. In addition to this automated filtering technique, a small percentage of the remaining data points are manually filtered because cloud contamination is obviously present. The efficacy of this cloud-filtering algorithm is unknown, and it has not been quantitatively compared with other algorithms used in operational systems, such as AERONET.[20] Circumstantial evidence in the form of comparisons of the filtered FRSR time series against Microtops data, which are manually filtered by the instrument operator, suggests that it performs well under most circumstances.

The uncertainty in FRSR measurements has been rigorously analyzed with data- and error-propagation models.[14] The uncertainty in $\tau_{\lambda A}$ is approximately 0.03 at low zenith angles and 0.02 at high zenith angles. This uncertainty can degrade to 0.04 at low solar zenith angles if the gain of the instrument drifts significantly over the duration of a deployment.

B. Total Sky Imager

It is often convenient to have a visual reference from which to evaluate sky condition. A TSI provides continuous digitization of the hemispheric sky condition and computes cloud amount for each image.[21] The TSI used on the R/V Ronald H. Brown during the ACE-Asia was a modified version of the Model 880 device manufactured by Yankee Environmental Systems, Inc. For ship operation, a spherical dome control system that compensates for ship motion was designed at Brookhaven National Laboratory. The dome rotates in response to continuous information about ship heading such that a black Velcro strip always occludes the Sun. The TSI software produces both images and a quantitative estimate of cloud fraction for each minute of the day, although only the visual images are used in this paper.

3. Sunphotometer Data-Quality Evaluations and Comparisons

A key problem in the analysis of the aerosol optical data collected during the ACE-Asia is arriving at an estimate of the time series of $\tau_{\lambda A}$ when it is being measured by several instruments with different calibrations, spectral bandpasses, and complicated uncertainties. A fundamental issue is the calculation of α, often computed by use of only two spectral bands, when the measurements of $\tau_{\lambda A}$ from different instruments have different spectral bandpasses. To circumvent this problem, we used a fit to all values of $\tau_{\lambda A}$ to compute α. As discussed below, however, this α fitting technique produces uncertainty artifacts that must be considered in this analysis. There is a fundamental disagreement in the value of $\tau_{\lambda A}$ measured by the Simbad and FRSR bands when the band center is $<$440 nm, which has serious implications for the calculation of α. Analysis of the FRSR data in the 410-nm band showed them to be noisy and of low quality, consistent with the performance of this band in other experiments. There are relatively fewer measurements from SimbadA and PMEL Microtops (discussed below) than from the other instruments. Therefore we excluded data from the $<$440-nm bands to avoid introducing unknown biases that might result from occasional inclusion of data from $<$440 nm from only two instruments in the calculation of α.

To form the necessary data set for a direct comparison of the measurements from the five instruments we prescribe a 15-min window surrounding the individual measurement from one instrument. A search through the data set is performed to identify measurements from the other instruments

(similar bands, within 10 nm) that fall within this window. The temporally closest measurement within the 15-min window is used as the comparison data point. Comparisons of $\tau_{490-500A}$ and α are shown as scatterplots (Figs. 2–5). Although only $\tau_{490-500A}$ scatterplots are shown, comparisons for other channels' values of $\tau_{\lambda A}$ show similar relationships when the instruments are compared (Table 3). The PMEL Microtops data have been omitted from the scatterplots because the number of comparison data points after pointing uncertainties have been filtered is 1–2 orders of magnitude lower than for the other comparisons (these data are included in the tabulated results).

The $\tau_{490-500A}$ scatterplots for the hand-held units show data with relatively small scatter and points that lie close to a line with a slope of 1 (Fig. 2). Although the scatter is slightly larger, the agreement in α for the hand-held units is also quite good, especially considering the larger uncertainty implicit in measurements of α, particularly at low $\tau_{\lambda A}$ (Fig. 3). Whereas a multiband line fit was used to compute α in this paper, one can demonstrate this source of uncertainty by propagating the uncertainty in a simple two-wavelength calculation of α. This uncertainty is expressed as

$$\sigma_\alpha{}^2 = \underbrace{[\ln(\lambda_1/\lambda_2)]^{-2}}_{\text{Band Separation}} \quad \underbrace{[(\sigma_{\tau_{\lambda 1}}/\tau_{\lambda 1})^2 + (\sigma_{\tau_{\lambda 2}}/\tau_{\lambda 2})^2]}_{\text{AOT}}, \quad (2)$$

where $\sigma_\alpha{}^2$ is the α uncertainty and AOT is the aerosol optical thickness. Equation (2) is similar in form to previously published versions.[8,22] As indicated in Eq. (2), $\sigma_\alpha{}^2$ is function of the solar zenith angle through its dependence on $\sigma_{\tau_\lambda}{}^2$ and is proportional to the inverse square of $\tau_{\lambda A}$ (the AOT term), a characteristic that contributes to scatter in the α comparisons. We illustrate this by plotting the ratio of α from each instrument versus the average $\tau_{490-500A}$ for the two instruments (Fig. 4). The Microtops–Simbad plot, which is a particularly good example of this sunphotometer's uncertainty property, demonstrates increased scatter in the α ratio when $\tau_{490-500A}$ becomes small. Calculations of $\sigma_\alpha{}^2$ for various situations show that $\sigma_\alpha{}^2$ ranges from 0.3 to 0.5 in extremely clean air masses, depending on the solar zenith angle, to 0.01 to 0.03 in fairly polluted air masses.[13] The same sources of uncertainty in $\sigma_\alpha{}^2$ can influence values of $\sigma_\alpha{}^2$ retrieved by satellite data with low values of $\tau_{\lambda A}$.[22]

Another issue in the α comparisons that is not demonstrated by the two-wavelength error-propagation calculation shown in Eq. (2) arises from the use of a line fit to the $\tau_{\lambda A}$ data to compute α. The uncertainty in this method is sensitive to the number of channels and to the distribution of channels across the visible and near-infrared spectra that is used in the line fit. Ideally, comparisons of instruments should be made by use of line fits based on the same number of channels and approximately the same channel locations across spectrum. Moreover, the band-separation term in Eq. (2) shows that the separation between the two bands contributes to uncertainty. This sensitivity is exhibited when a line fit is used.

The broader comparison of all channels (Table 3) shows that, with few exceptions, the measurements from the hand-held sunphotometers agree well across all channels. Considering the most statistically significant comparison (SIMBIOS Microtops and Simbad, which have 663 measurement comparisons), $>89\%$ of the $\tau_{\lambda A}$ observations agree within published uncertainties, correlation coefficients are large (~ 0.99), biases range from 0 to -0.03, and the percent root-mean-square (RMS) error is $<10\%$. The percent RMS error is relative to the average value of the comparison points. Similarly, the comparisons of α are encouraging even though larger errors are to be expected because they represent the compounded errors from the individual channels. Both Simbad and SimbadA seem to compare less favorably with the Microtops in the near-infrared channels in term of percent RMS error for reasons that are not clear. Comparisons between the hand-held units and the FRSR are less encouraging, in general, which is to be expected because the FRSR is deployed for long periods and is automated. The percent RMS uncertainties are $>15\%$ in most cases, although correlation coefficients remain large. The RMS uncertainties in the comparisons reflect the published uncertainties of the instruments, which suggest that their uncertainty characteristics of the instruments are well characterized.

The FRSR–hand-held comparison scatterplots (Fig. 5) show systematic FRSR underestimation of $\tau_{490-500A}$ when $\tau_{490-500A} > 0.5$. This disagreement is traced to difficulties with the shadow-band technique as a result of enlargement in the solar aureole in highly polluted air masses and is consistent across all bands. Images from the TSI illustrate the two extremes in sky condition encountered during the cruise: a clean, maritime air mass over the Northern Pacific Ocean [Fig. 6(a)] and a highly polluted air mass over the Sea of Japan [Fig. 6(b)]. The figure shows extremely blue sky and modest whitening at the horizon in the clean air mass. In contrast, in the polluted air mass the horizon has a brownish color and that the entire sky appears to be dull and whitened. The reduction in total irradiance between the two air masses is graphically illustrated by comparison of the brightness of the ship's superstructure in the two images. The solar aureole, which is the faintly colored luminous ring that surrounds the Sun's disk through the haze, is significantly larger and brighter in the polluted air mass.

The enlarged solar aureole in highly polluted air masses (and when thin cirrus is present) necessitated an adjustment in the FRSR sweep-level processing. This is so because the direct beam irradiance is computed from the difference between the shadow irradiance and the edge irradiance, which is the irradiance just before the occulting band reaches the edge of the solar disk.[13] When an air mass is clean and the solar aureole is minimal, well-defined edge-

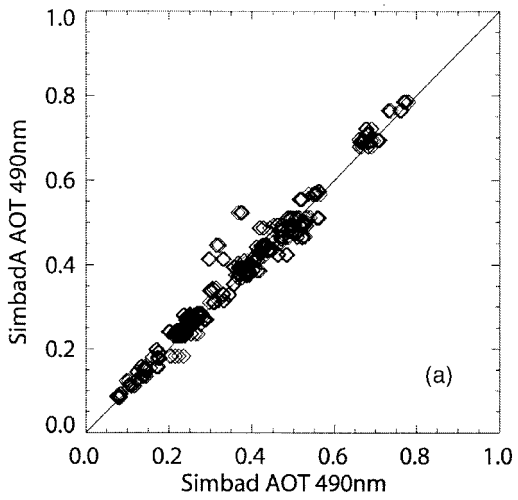

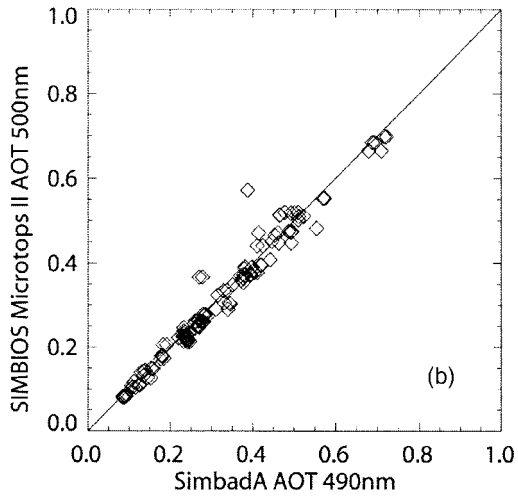

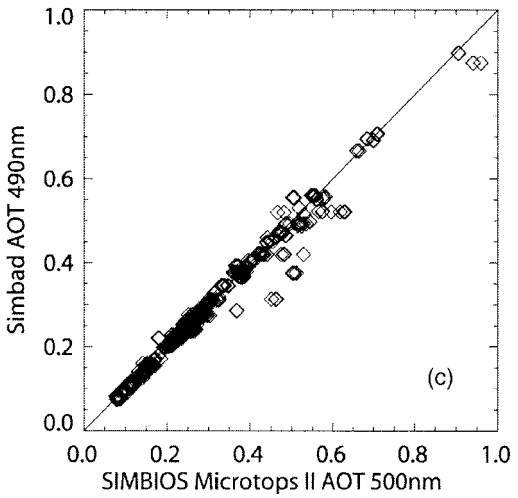

Fig. 2. Comparison plots of $\tau_{\lambda A}$ at the specified wavelength for the hand-held marine sunphotometers. Each data point represents a direct comparison between the two instruments during 15-min windows, and the instruments are never more than 83.5 m apart. The total number of comparison points is indicated beneath each figure, along with the percentage that agreed within uncertainty: (a) Simbad versus SimbadA 490-nm channels, (b) SimbadA 490-nm versus SIMBIOS Microtops 500-nm channels, (c) SIMBIOS Microtops 500-nm channel versus Simbad 490-nm channel. AOT, aerosol optical thickness.

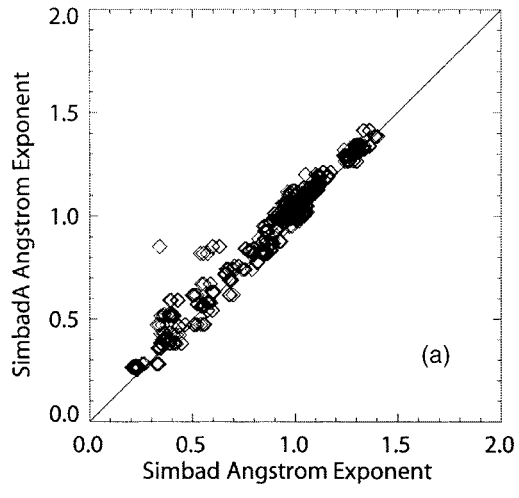

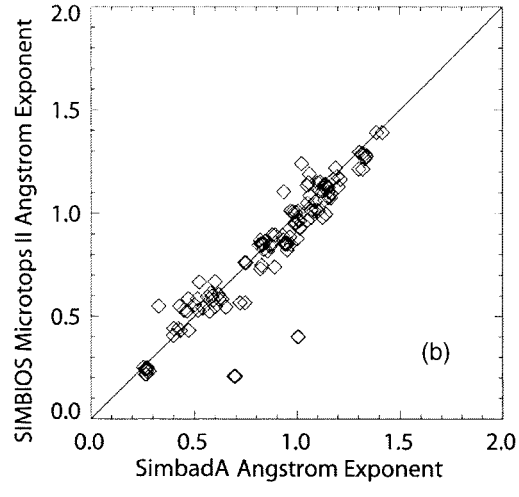

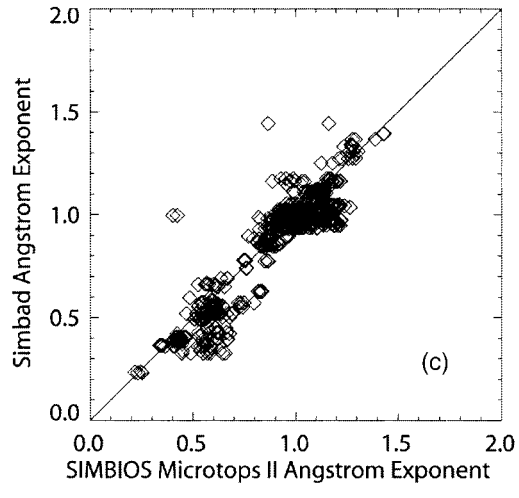

Fig. 3. Same as Fig. 2 but for α.

shadow irradiances can be determined from the individual sweeps within the 2-min data-collection window [Fig. 6(a)]. The variability from sweep to sweep is caused by ship motion and instrument response.[14] In contrast, the solar aureole is much less defined in the polluted air mass [Fig. 6(b)]. This situation requires that a nonlinear, curve-fitting

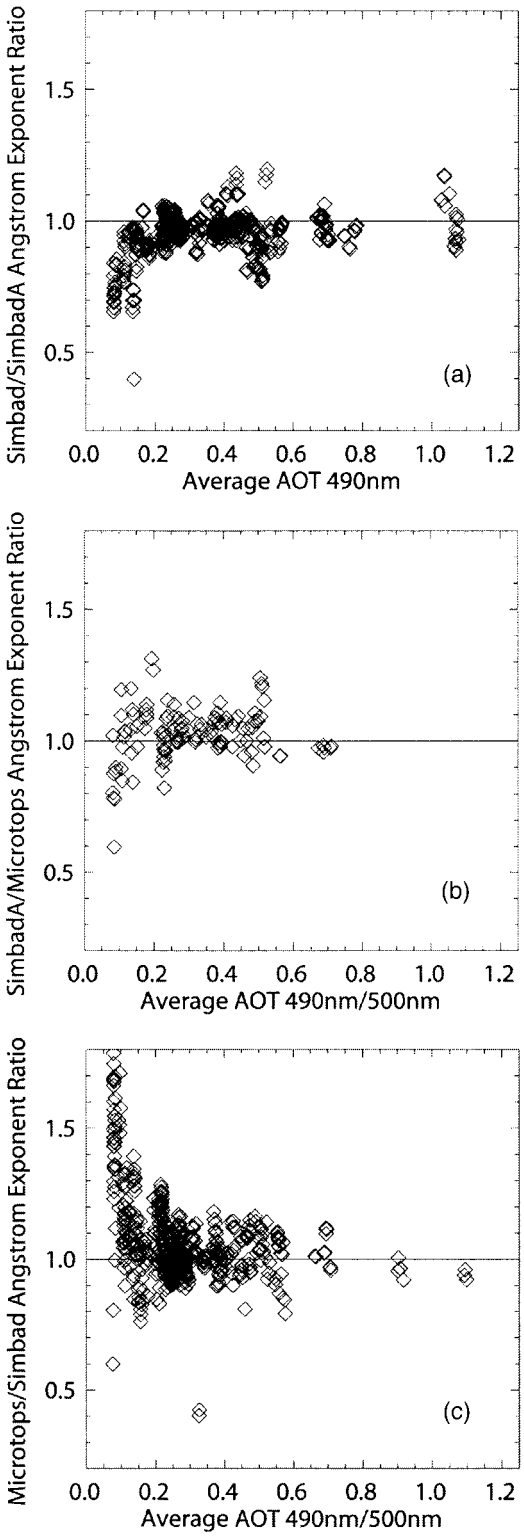

Fig. 4. Comparison plots of the ratio of α for the instruments listed on the *y* axis against the average $\tau_{\lambda A}$ (490- and 500-nm center wavelengths averaged together). Each data point represents a direct comparison between the two instruments during 15-min windows. The total number of comparison points is indicated beneath each figure, along with the percentage that agreed within uncertainty: (a) Simbad–SimbadA α ratio, (b) SimbadA–SIMBIOS Microtops α ratio, (c) SIMBIOS Microtops–Simbad α ratio.

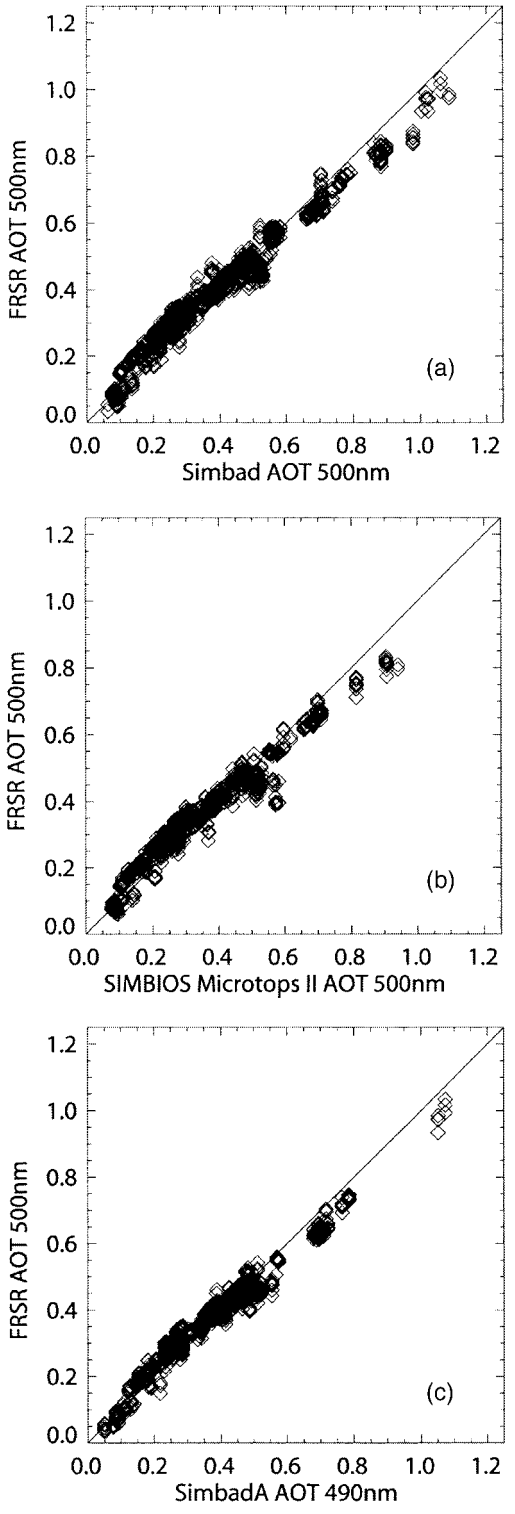

Fig. 5. Comparison plots of $\tau_{\lambda A}$ at the specified wavelength for the FRSR and hand-held marine sunphotometers. Each data point represents a direct comparison between the two instruments during 15-min windows. The total number of comparison points is indicated beneath each figure, along with the percentage that agreed within uncertainty. (a) Simbad 490-nm versus FRSR 500-nm channel, (b) SIMBIOS Microtops 500-nm channel versus FRSR 500-nm channel, (c) Simbad 490-nm channel versus FRSR 500-nm channel.

Table 3. Statistical Summary of Instrument Intercomparisons[a]

	% Within Error	Corr. Coeff.	Bias[b]	RMS	% RMS
MTNA to SMBD; number of points, 663					
MTNA–SMBD–AOT440	89.6	0.9887	−0.0210	0.0330	8.7
MTNA–SMBD–AOT500	94.7	0.9912	−0.0051	0.0211	5.5
MTNA–SMBD–AOT670	94.1	0.9922	−0.0107	0.0199	7.3
MTNA–SMBD–AOT870	89.3	0.9875	−0.0096	0.0218	9.6
MTNA–SMBD–ANG	98.8	0.9204	−0.0335	0.1156	
MTNO to MTNA; number of points, 10					
MTNO–MTNA–AOT440	80.0	0.9985	0.0186	0.0213	4.3
MTNO–MTNA–AOT500	80.0	0.9963	0.0033	0.0151	2.6
MTNO–MTNA–AOT675	100.0	0.9988	0.0132	0.0151	4.8
MTNO–MTNA–AOT870	90.0	0.9980	0.0160	0.0182	7.7
MTNO–MTNA–ANG	100.0	0.9805	−0.0502	0.0697	
MTNO to SMBD; number of points, 13					
MTNO–SMBD–AOT440	84.6	0.9964	0.0216	0.0295	4.7
MTNO–SMBD–AOT500	69.2	0.9941	0.0238	0.0333	7.0
MTNO–SMBD–AOT670	69.2	0.9968	0.0245	0.0300	7.5
MTNO–SMBD–AOT870	38.5	0.9936	0.0339	0.0406	13.1
MTNO–SMBD–ANG	61.5	0.9646	−0.1046	0.1198	
MTNO to SMBA; number of points, 8					
MTNO–SMBA–AOT440	100.0	0.9975	0.0113	0.0178	3.3
MTNO–SMBA–AOT500	62.5	0.9971	0.0187	0.0282	7.7
MTNO–SMBA–AOT670	62.5	0.9967	0.0193	0.0234	7.9
MTNO–SMBA–AOT870	75.0	0.9905	0.0147	0.0230	7.5
MTNO–SMBA–ANG	100.0	0.9687	−0.0525	0.0685	
SMBA to MTNA; number of points, 128					
SMBA–MTNA–AOT440	89.1	0.9839	0.0134	0.0332	9.3
SMBA–MTNA–AOT500	89.1	0.9783	−0.0033	0.0325	9.6
SMBA–MTNA–AOT670	91.4	0.9665	0.0041	0.0348	12.7
SMBA–MTNA–AOT870	81.2	0.9497	0.0166	0.0433	21.3
SMBA–MTNA–ANG	96.9	0.9271	−0.0340	0.1199	
SMBD to FRSR; number of points, 1102					
SMBD–FRSR–AOT500	72.4	0.9851	0.0094	0.0455	17.4
SMBD–FRSR–AOT680	74.4	0.9878	−0.0246	0.0435	17.3
SMBD–FRSR–AOT870	87.4	0.9870	−0.0053	0.0330	14.7
SMBD–FRSR–ANG	66.0	0.6301	0.3412	0.4790	
SMBA to SMBD; number of points, 162					
SMBA–SMBD–AOT443	95.1	0.9903	−0.0079	0.0289	7.7
SMBA–SMBD–AOT490	95.1	0.9929	−0.0089	0.0242	7.2
SMBA–SMBD–AOT560	94.4	0.9941	−0.0083	0.0208	7.9
SMBA–SMBD–AOT670	83.3	0.9945	−0.0087	0.0192	8.3
SMBA–SMBD–AOT870	85.8	0.9944	0.0031	0.0163	8.7
SMBA–SMBD–ANG	98.8	0.9690	−0.0459	0.0921	
SMBA to FRSR; number of points, 177					
SMBA–FRSR–AOT410	52.5	0.9781	−0.0447	0.0610	21.0
SMBA–FRSR–AOT500	83.6	0.9875	0.0008	0.0317	11.8
SMBA–FRSR–AOT615	88.7	0.9890	0.0168	0.0309	14.9
SMBA–FRSR–AOT680	75.7	0.9903	−0.0313	0.0396	21.2
SMBA–FRSR–AOT870	92.7	0.9913	−0.0005	0.0201	11.7
SMBA–FRSR–ANG	75.1	0.4645	0.3355	0.5127	
MTNO to FRSR; number of points, 16					
MTNO–FRSR–AOT500	87.5	0.9962	0.0001	0.0316	8.1
MTNO–FRSR–AOT680	93.8	0.9976	−0.0189	0.0281	5.6
MTNO–FRSR–AOT870	100.0	0.9983	0.0039	0.0131	6.5
MTNO–FRSR–ANG	100.0	0.9803	0.0835	0.1057	
MTNA to FRSR; number of points, 763					
MTNA–FRSR–AOT500	69.9	0.9710	0.0174	0.0394	16.4
MTNA–FRSR–AOT680	79.7	0.9729	−0.0246	0.0384	20.0
MTNA–FRSR–AOT870	92.5	0.9738	−0.0044	0.0277	13.1
MTNA–FRSR–ANG	73.8	0.4425	0.3700	0.4838	

[a]Abbreviations: MTNA, NASA Simbios Microtops; MTMO, PMEL Microtops; SMBD, Simbad; SMBA, SimbadA; ANG, Ångström coefficient.

[b]Bias, second instrument listed; first instrument listed for any pair of comparisons.

scheme be employed to determine the edge irradiance. Most importantly, the state of the sky as inferred from individual sweep data from the FRSR and visual evidence from the TSI clearly suggest that multiple scattering cannot be ignored in this highly polluted environment. Despite improvements in the $\tau_{490-500A}$ shadow-band algorithm, this bias still exists, though it is considerably smaller than the bias associated with the algorithm used before this analysis. Similar biases exist in the other channels, so caution must be exercised when one is interpreting FRSR measurements if $\tau_A > 0.5$.

The FRSR α values and their associated uncertainties as calculated by Eq. (2) agree more than 69% of the time compared with those from Microtops and more than 72% compared with those from Simbad and SimbadA (Table 3), although the plots suggest that the FRSR has a tendency to overestimate α (Fig. 7). The reason for this α overestimation tendency is most likely a slight bias in the $\tau_{\lambda A}$ measurements on one end or the other of the visible spectrum. Information presented in Table 4 suggests that the problem may lie in the short-wavelength end of the spectrum (610–500 nm) and may involve sweep-level processing caveats. This α overestimation tendency is a subject of ongoing research, and further refinement of the sweep-level processing may correct this problem. Plots of the ratio of α values of the various instruments (Fig. 8) suggest that FRSR discrepancies are particularly acute in clean air masses ($\tau_{490-500A} < 0.2$), although much of this apparent discrepancy is due to the uncertainty characteristics of α, as discussed above. Even so, it is doubtful that the degradation in the α comparisons is entirely due to the uncertainty considerations in α. The reasons for this α bias are not clear, though unknown caveats in the sweep level processing may be partly responsible.

To summarize the composite results for each instrument versus all other instruments, a sample-number-weighted average of the percent agreement is computed (Table 4). From the matrix containing the percent agreement for each instrument combination in each overlapping band (Table 3), a sample-number-weighted average of the percent agreement is calculated. This serves the purpose of identifying suspect channels based on intrainstrument comparisons. The results show that there is excellent agreement in $\tau_{\lambda A}$ measurements collected with the hand-held sunphotometers (>75%), although weighted average percent agreements are notably lower for the SimbadA and the FRSR. Excluding the 410-nm channel, as discussed above, all instruments agree within uncertainties of at least 72% of the time for $\tau_{\lambda A}$ and ~70% for α. If the PMEL Microtops, which has a small number of comparison points, is used and an atypical measurement protocol is excluded, the composite hand-held sunphotometer agreement rises to ~82%.

4. Creating a Time Series of $\tau_{\lambda A}$

To illustrate some of the basic caveats involved in arriving at a best-estimate time series of $\tau_{\lambda A}$ for the ACE-Asia cruise data, two time series of the cloud-filtered data from the various instruments collected during two periods are analyzed (Fig. 9). The ship was traversing clean maritime air during the first day (29 March 2001) and a polluted continental air mass during the second (9–10 April 2001). Inspection of the time series of τ_{500A} [Figs. 9(a) and 9(b)] suggests a larger variability in the FRSR data than in the hand-held instruments in the clean air mass but no systematic offset. In contrast, the FRSR measurements of τ_{500A} are systematically lower in the polluted air mass than the hand-held values. This offset is due to a deficiency in the FRSR technique in highly polluted air masses, as discussed above. There is considerable variability in the measurements of α in the clean air mass and excellent agreement in the polluted air mass. Considering the known uncertainties in measurements of α, which are of the order of 0.6 in a clean maritime air mass,[14] the measurements shown in the clean air mass on 29 March, despite their spread, actually agree within uncertainties. Evidence presented above suggests that agreement within uncertainties does not always occur (Fig. 8).

These two days are indicative of the nature of the multiple-instrument time series through the range of conditions encountered aboard the R/V Ronald H. Brown during the ACE-Asia and on many other cruises. How to produce a best estimate is a complex issue for many reasons. Ideally, a weighted average could be formed by use of weights that are formulated on the basis of measurement uncertainty. Although the estimated accuracy of the hand-held sunphotometers is 0.012–0.019, it is nearly impossible to complete a rigorous uncertainty evaluation because the sun-pointing errors likely depend on a complicated relationship among observer dexterity, the size of the ship, and the state of the sea. Notwithstanding, the FRSR uncertainty is probably more accurately known than the uncertainties of the hand-held sunphotometers, and it is not impossible that the uncertainty of the hand-held sun photometers would be more like that of the FRSR if the sun-pointing errors could be rigorously quantified. Another important characteristic of the uncertainty that is not considered in our analysis (even in the rigorous FRSR analysis) is the effect of averaging on the random-noise element of the measurements. Orientation error, whether it be mechanical or human-induced, is likely to be random and therefore subject to the rules of signal processing. The signal-to-noise ratio of a signal containing white noise is increased by a factor of $n^{-0.5}$, where n is the number of independent samples that are averaged. This mathematical characteristic of noise produces two additional complications: (1) one needs to know what constitutes an independent sample and (2) the FRSR collects at least an order of magnitude more samples than the hand-held sunphotometers. Sample independence is almost certainly a function of the sea state and could be determined by calculation of the autocorrelation function, but it would be difficult to compute this

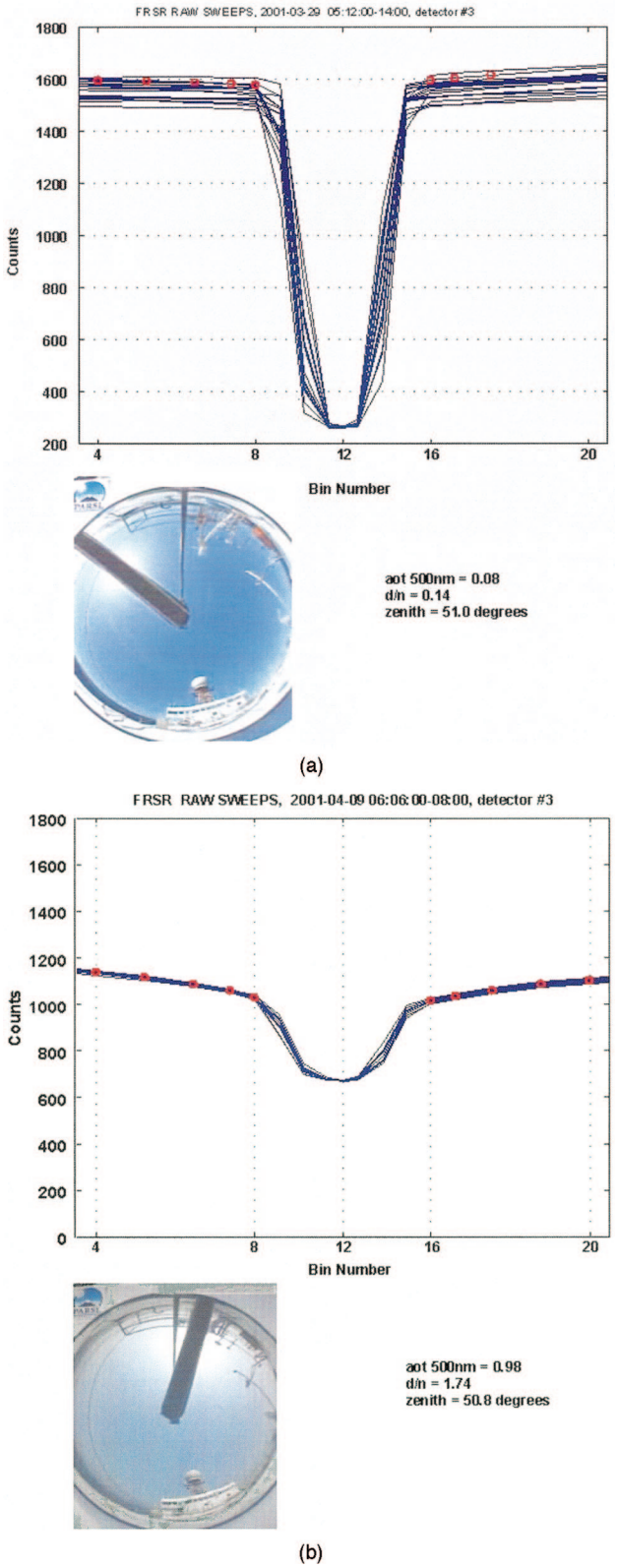

Fig. 6. (a) Time series of voltage counts from the FRSR for each sweep that passed quality control during a 2-min sampling window. These individual sweeps are used to determine the direct-normal irradiance. Red circles, voltages selected by the FRSR processing as representative of the edge voltage.[13,14] Visible sky images from the TSI for one of the individual sweeps from (a) the Northern Pacific Ocean in a clean air mass ($\tau_{\lambda A} = 0.08$ at 500 nm) and (b) the polluted air mass above the Sea of Japan ($\tau_{\lambda A} = 0.98$ at 500 nm).

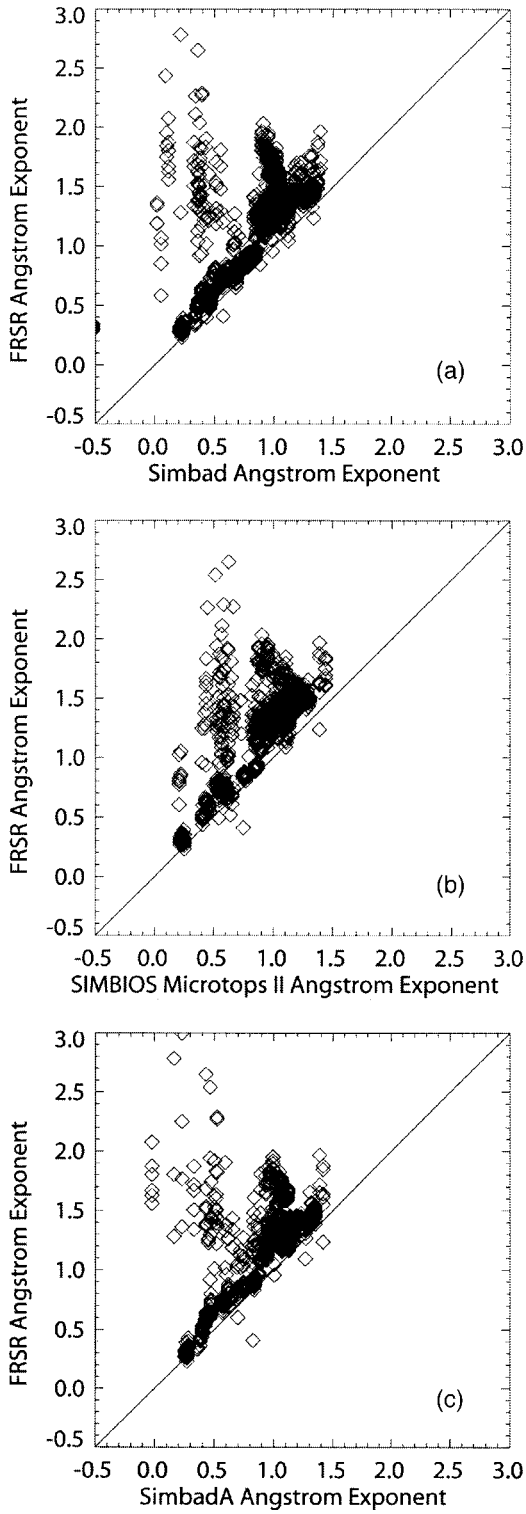

Fig. 7. Comparison plots of α at the specified wavelength for the FRSR and the hand-held marine sunphotometers. Each data point represents a direct comparison between the two instruments during 15-min windows: FRSR versus (a) Simbad, (b) SIMBIOS Microtops, and (c) SimbadA.

function for a real deployment on a ship for which the motion is sensitive only not to the sea state but also to the ship's moment of inertia. Thus it is not easy to

Table 4. Percentage of ACE-Asia Concurrent Measurements That Fall Within Calculated Uncertainties[a]

Wavelength (nm)	Instrument				
	MTNA	MTNO	SMBD	SMBA	FRSR
410				52.5	52.5
440	89.4	87.1	90.6	92.6	
500	82.0	76.6	81.9	88.6	72.6
560			94.4	94.4	
615				88.7	88.7
670	86.9	78.7	81.8	82.3	76.6
870	90.2	76.6	87.6	86.9	89.8
Ang	86.5	89.4	79.9	89.5	69.9

[a]Abbreviations: MTNA, NASA Simbios Microtops; MTMO, PMEL Microtops; SMBD, Simbad; SMBA, SimbadA; Ang, Ångström exponent.

determine how much the signal-to-noise ratio is increased by averaging, which further complicates the uncertainty estimates for the sunphotometers used in this study.

The issue of marine sunphotometer uncertainty is sufficiently complex that an uncertainty-weighted approach to producing a best estimate seems untenable at present. There is enough internal consistency in the measurements, however, to suggest that one can form daily averages and statistics of $\tau_{\lambda A}$ and α by combining the data from all five instruments with equal weighting. This procedure produces a time series of the daily geometric mean, geometric standard deviation, and extremes through the duration of the experiment. The geometric mean, rather than the arithmetic mean, is used because statistics of $\tau_{\lambda A}$ from long-term studies show a log normal distribution as opposed to the normal distribution of α.[23,24] The time series are hereafter referred to as the averaged time series of $\tau_{\lambda A}$ or α (Fig. 10). A sampling issue is the relatively large number of data points generated by the FRSR relative to the hand-held sunphotometers, whereupon the averaged time series is biased toward the FRSR measurements. Results presented above suggest this bias has little effect under most circumstances but may have a minor effect in highly polluted conditions owing to the difficulties encountered in the FRSR sweep processing.

The averaged time series quantifies a wide variety of conditions, including exceptional pollution in coastal areas (Figs. 2 and 10). Aerosols are being sampled by a ship moving in a trajectory that is independent of wind flow and are therefore encountering mesoscale features such as limiting streamlines in the wind field. Such streamlines can lead to sharp aerosol distribution gradients, which occurred in this case during the latter, highly polluted portion of the cruise. Days with smaller values of $\tau_{\lambda A}$ show low variability, whereas polluted conditions have extremely high variability that cannot be adequately sampled by use of sparse data from the hand-helds. Days 99 and 100 are examples of variable conditions encountered during these polluted conditions. The converse is true for α, as measurements are far more accurate

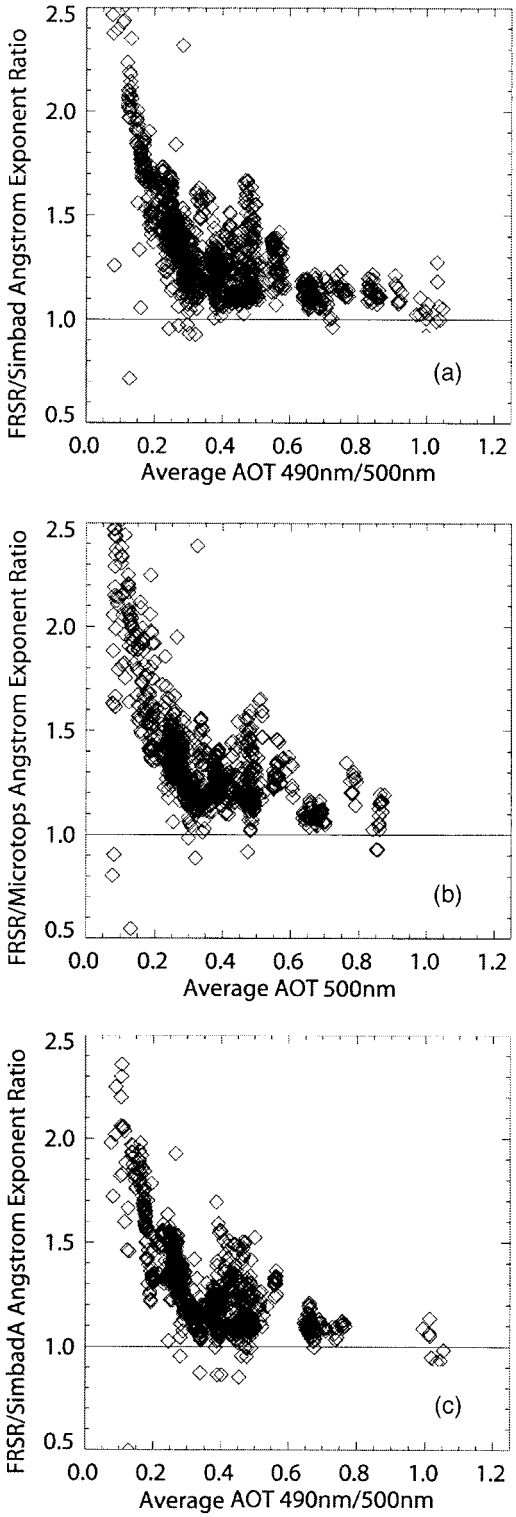

Fig. 8. Comparison plots of the ratio of α for the instruments listed on the y axis against the average $\tau_{\lambda A}$ (490- and 500-nm center wavelengths averaged together). Each data point represents a direct comparison between the two instruments during 15-min windows. The total number of comparison points is indicated beneath each figure, along with the percentage that agreed within uncertainty. (a) Simbad–SimbadA α ratio, (b) SimbadA–SIMBIOS Microtops α ratio, (c) SIMBIOS Microtops–Simbad α ratio.

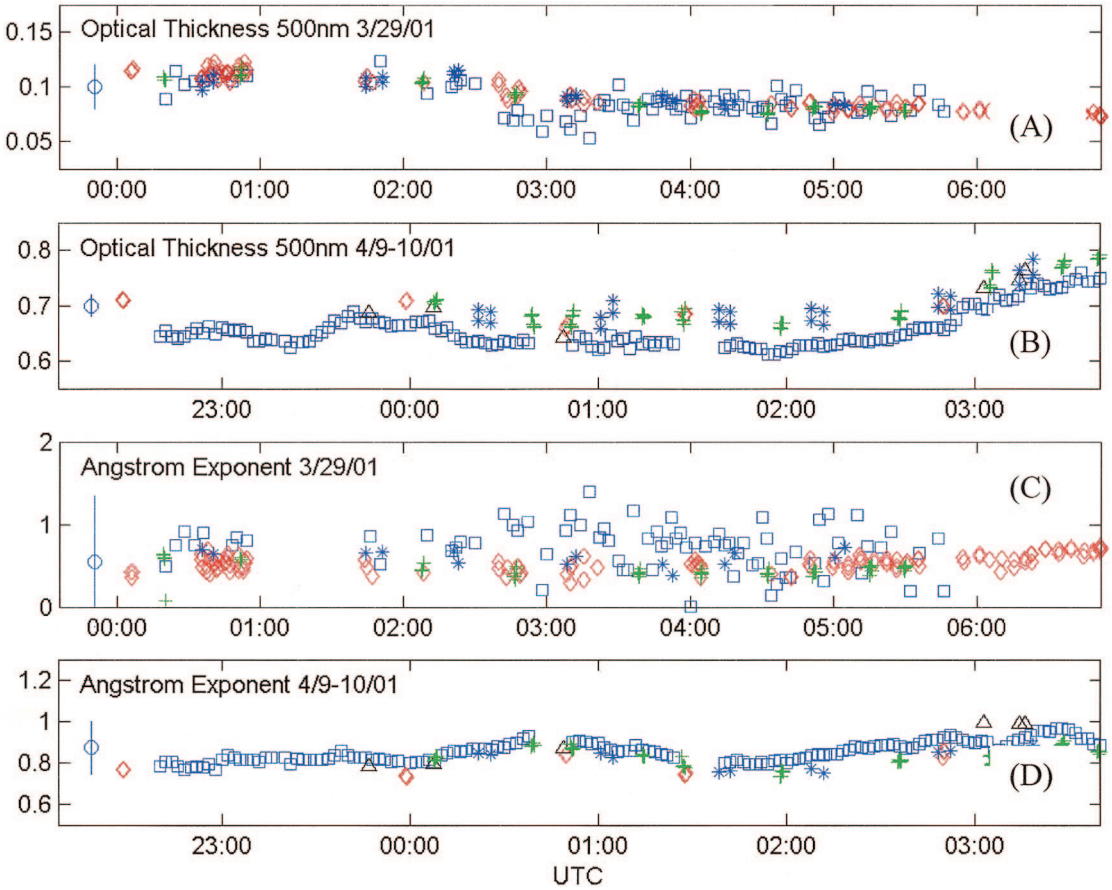

Fig. 9. (a) Time series of $\tau_{\lambda A}$ for 29 March 2001 from the FRSR (blue squares), Microtops with custom algorithm (red diamonds), Simbad (green pluses), SimbadA (blue asterisks), and Microtops without the custom algorithm (black triangles). Blue circles with vertical lines represent typical uncertainties for these measurements: (b) as in (a) but for 9–10 April 2001; (c) as in (a) but for α; (d) as in (b) but for α.

in polluted conditions. Because the handhelds are not so exposed to the elements and typically have been calibrated more recently than the FRSR, they tend provide a more accurate measurement of $\tau_{\lambda A}$ and α. Conversely, the FRSR is useful for evaluation of aerosol homogeneity throughout the period to be averaged.

Frequency distributions of $\tau_{\lambda A}$ and α for the entire experiment period reveal some systematic biases. The frequency distributions of $\tau_{490\text{–}500A}$ and τ_{870A} for the experiment are remarkably similar despite the different sampling strategies of the FRSRs and handhelds (Fig. 11). The most notable feature of the histograms is the relatively larger frequency of measurements with of $\tau_{\lambda A} < 0.2$ indicated by the handheld sunphotometers. Although a large uncertainty is assigned to measurements when $\tau_{\lambda A} < 0.2$, which complicates the interpretation of this region of air mass phase space, uncertainty arguments are not sufficient to explain the observed biases. Despite the systematic underestimate of $\tau_{\lambda A}$ by the FRSR in extremely polluted conditions, as demonstrated above, the frequency distributions of $\tau_{\lambda A}$ suggest that these highly polluted conditions are observed so infrequently that their effect on the experiment statistics is minimal.

In contrast to the excellent agreement in the histograms of $\tau_{\lambda A}$, histograms of α reveal significant biases [Fig. 11(c)]. Specifically, the frequency distributions from the FRSR and the hand-held sunphotometers have peaks at different values of α. This offset cannot be attributed to the observed differences in the frequency distributions of $\tau_{\lambda A}$ when $\tau_{\lambda A} < 0.2$, as described above, because α is typically small ($\alpha < 0.5$) in clean maritime air masses. Moreover, the large uncertainty associated with computing α in a clean, maritime air mass makes it impossible to distinguish between the two peaks in the frequency distribution. The α measurements agree within uncertainty when $\alpha < 0.5$. The effect of the observed differences in the frequency distributions of $\tau_{\lambda A}$ when $\tau_{\lambda A} < 0.2$ is confined to the phase space in the α histogram where $\alpha < 0.5$. Therefore the clean maritime air mass bias cannot explain the observed offset in the peaks of the frequency distributions of α when $\alpha > 0.5$ [Fig. 11(c)]. In this circumstance, the histograms show that the FRSR has a peak in its α frequency distribution at values that are a factor of 0.3 larger than the peak for the hand-held units. In addition, there is a tail in the FRSR frequency distribution when $\alpha > 1.5$ that does not exist in the frequency distributions of the hand-held units. Nota-

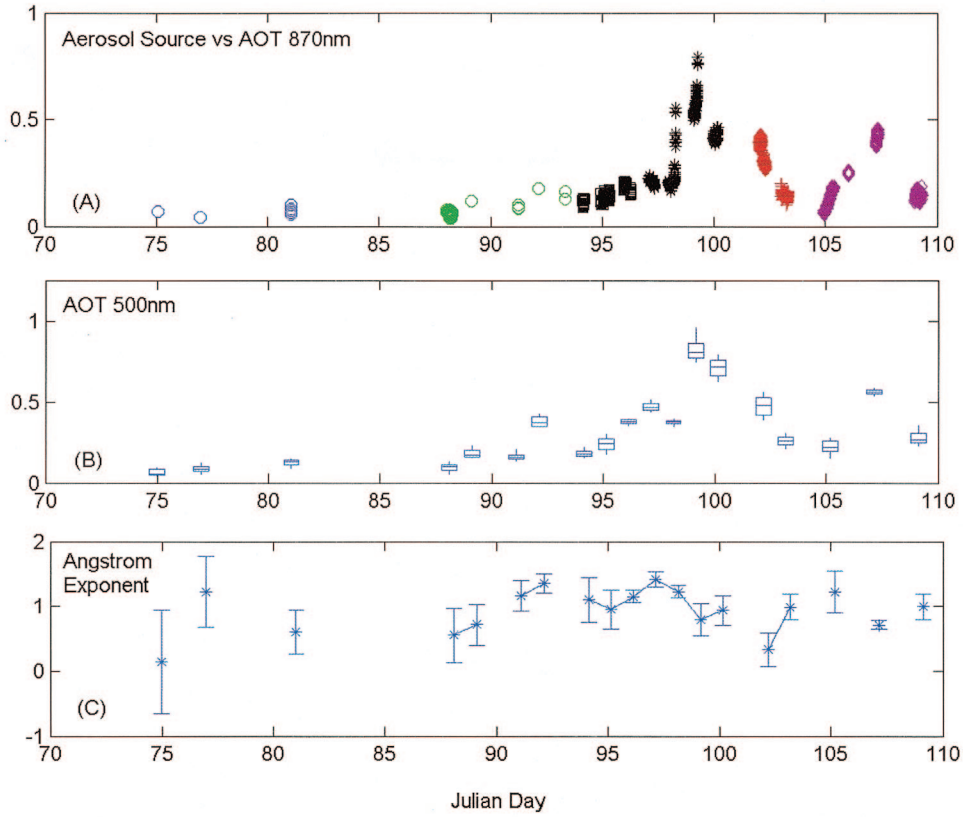

Fig. 10. (a) Plot of $\tau_{\lambda A}$ at 870 nm classified by trajectory-based air mass type. The air masses are plotted according to the color codes in Fig. 1 and with different symbols. (b) Time series of the geometric statistics of cloud-filtered $\tau_{\lambda A}$ at 500 nm for a 1-h window near local noon. The whisker plots show the geometric mean (center bar) and the geometric standard deviations (upper and lower bounds of box), and the lines above and below represent the maximum and minimum observed values: (c) as in (b) but for 670 nm; (d) as in (b) but for 870 nm; (e) α for the experiment period.

bly, the two frequency distributions exhibit a similar bimodal shape, though the distribution for the hand-held units is considerably narrower.

One reason for the differences in the frequency distributions of α is the underlying method that is used to compute α [Figs. 11(c) and 11(d)]. When α is computed by the two-band method [Fig. 11(d)], the frequency distributions of α for the FRSR and the hand-held sunphotometers show considerably better agreement and the widths of the two frequency distributions are similar, though the peaks in the two distributions remain offset. There is some overlap in the distributions surrounding the peaks that is not present when the line-fitting method is used [i.e., the peaks are narrower; Fig. 11(c)]. The differences observed when the line-fit method is used may be generated by any or all of the following conditions: (1) differences in the spectral resolution of the information in the 560–680-nm range supplied by the hand-held sunphotometers and by the FRSR, (2) one or more poorly calibrated channels in the 560–680-nm range, (3) technique-related biases that are observed only in the 560–680 nm range, and (4) inability to include the <440-nm channels in our analysis owing to fundamental intrainstrument disagreement. This analysis shows that the statistical distribution of α during this experiment is different for the combined data from the hand-held sunphotometers and the FRSR and that these differences may arise from a combination of factors.

To adequately describe the aerosol optical conditions at a given time during the ACE-Asia cruise aboard the Ronald H. Brown, or on any cruise, it is essential to understand the absolute values of $\tau_{\lambda A}$ and α as well as the geometric variability for an appropriate window of time surrounding the observation. This criterion dictates that the most comprehensive characterization of the aerosol conditions will be made when complementary measurements are made with the FRSR and hand-held instruments. Failure to collect complementary data may result in unintended biases in the data set, depending on the application. For example, accurate aerosol optical measurements from a hand-held sunphotometer may well represent the current conditions but fail to capture the local variability in the air mass. Conversely, continuous measurements from a FRSR may provide an excellent survey of aerosol variability but a less-accurate measurement of $\tau_{\lambda A}$ and α owing to a degraded calibration. The FRSR also provides important supporting measurements in the form of a dissection of the global irradiance into its direct-normal and diffuse components. Clearly, a complementary measurement effort with dutiful calibration and

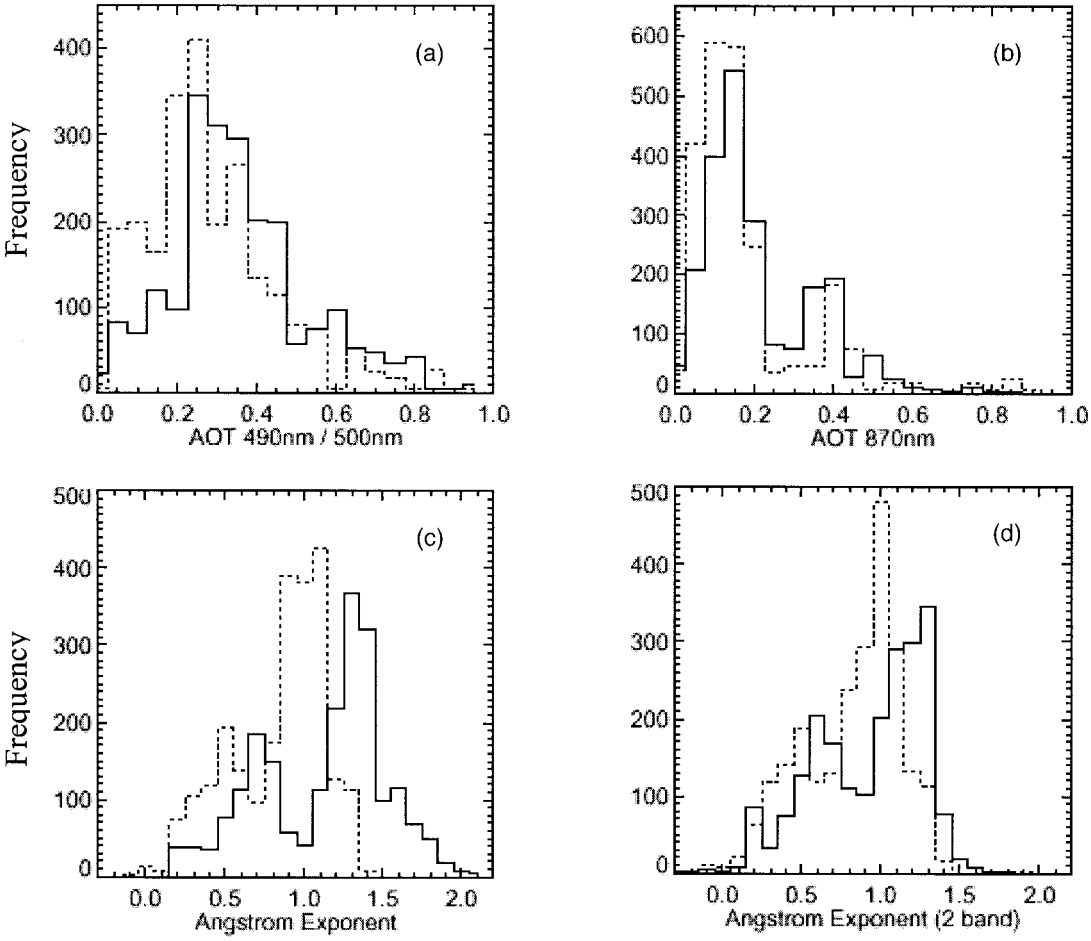

Fig. 11. Histograms of $\tau_{\lambda A}$ and α for the R/V Ronald H. Brown cruise during the ACE-Asia. Dashed lines are histograms of the hand-held data; solid lines, of the FRSR data. The bin width for $\tau_{\lambda A}$ is 0.05, and the bin width for α is 0.1. (a) $\tau_{490\text{–}500A}$ (490- and 500-nm center wavelengths averaged together), (b) τ_{870A}, (c) α computed by fitting of a line through all measurements of $\tau_{\lambda A}$, (d) α computed by use of only two bands ($\tau_{490\text{–}500A}$ and τ_{870A}).

uncertainty consideration is the most accurate approach to marine sunphotometry.

5. Discussion and Conclusions

The results presented in this study validate the premise that all hand-held sunphotometers that employ the rigorous SIMBIOS measurement and calibration procedures[17,18] produced similar measurements aboard the R/V Ronald H. Brown during the ACE-Asia cruise. As many conditions were encountered during the ACE-Asia, this conclusion is likely to be valid for most measurements at sea. Generally, the FRSR produced comparable results, although there is the potential for data-processing-related biases in high $\tau_{\lambda A}$ conditions. Results from this analysis have already inspired improvements in the FRSR data processing, and further improvement is likely.

The largest difference between the FRSR and hand-held instruments lies in the sampling rate. The FRSR sampling period is 2 min, whereas hand-held sampling rates are determined by the operator and sampling is typically much less frequent (several per hour under the best circumstances). The sampling rate is the fundamental issue in the selection of the appropriate device for a given application. The current SIMBIOS measurement protocol requires that a set of measurements (9–15, depending on the instrument) be made with properly configured instruments sequentially within an hour of satellite overpass.[17] The ACE-Asia FRSR data suggest that this sampling strategy may not be adequate in rapidly changing, highly polluted conditions. Increasing the number and regularity of hand-held sunphotometer measurements within an hour of satellite overpass increases the likelihood that aerosol conditions will be properly sampled. Operating the hand-held instruments with this protocol would be comparable in accuracy to the combination of high frequency FRSR and low-frequency, but well-calibrated, hand-held sunphotometer measurements. Such a sampling strategy is feasible only because of operator limitations for short periods such as a 1-h window required for satellite comparison.

The data collected aboard the R/V Ronald H. Brown during the ACE-Asia provided a rigid test of a number of marine sunphotometers and techniques. A wide range of aerosol conditions, including clean maritime conditions and highly polluted coastal environments, was encountered. The results of this study

suggest that the use of either hand-held or FRSR marine sunphotometers to measure $\tau_{\lambda A}$ will yield similar results if proper measurement protocols are used and if the instruments are properly calibrated.[25]

The first author dedicates his work on this manuscript to his brother Michael J. Miller (1962–2004). This work was funded by the DOE Atmospheric Radiation Measurement (ARM) Program and by the NASA Sensor Intercomparison and Merger for Biological Interdisciplinary Studies (SIMBIOS). This manuscript has been authored by the Brookhaven Science Associates, LLC under contract DE-AC02-98CH1-886 with the U.S. Department of Energy.

References

1. National Research Council, *Aerosol Radiative Forcing and Climatic Change* (National Academy Press, 1996).
2. R. B. Husar, J. M. Prospero, and L. L. Stowe, "Characterization of tropospheric aerosols over the oceans with the NOAA advanced very high resolution radiometer optical thickness product," J. Geophys. Res. **102,** 16,889–16,909 (1997).
3. M. A. Wetzel and L. L. Stowe, "Satellite-observed patterns in stratus microphysics, aerosol optical thickness, and shortwave radiative forcing," J. Geophys. Res. **104,** 31,287–31,299 (1999).
4. M. D. Chou, P. K. Chan, and M. Wang, "Aerosol radiative forcing derived from SeaWiFS-retrieved aerosol optical properties," J. Atmos. Sci. **59,** 748–757 (2002).
5. L. L. Stowe, H. Jacobowitz, G. Ohring, K. R. Knapp, and N. R. Nalli, "The advanced very high resolution radiometer (AVHRR) pathfinder atmosphere (PATMOS) climate dataset: initial analysis and evaluations," J. Climate **15,** 1243–1260 (2002).
6. S. A. Christopher and J. Zhang, "Shortwave aerosol radiative forcing from MODIS and CERES observations over the oceans," Geophys. Res. Lett. **29,** 1859–1863 (2002).
7. G. S. Fargion and J. L. Mueller, "Ocean optics protocols for satellite ocean color sensor validation: revision 2," NASA Tech. Memo 2000-209966 (NASA Goddard Space Flight Center, Greenbelt, Md., 2000).
8. A. K. Ångström, "Techniques for determining the turbidity of the atmosphere," Tellus **2,** 214–223 (1961).
9. A. Ångström, "The parameters of atmospheric turbidity," Tellus **16,** 64–75 (1964).
10. J. N. Porter, M. A. Miller, C. Motell, and C. Pietras, "Use of hand-held sun photometers for measurements of aerosol optical thickness at sea," J. Atmos. Ocean. Tech. **18,** 765–774 (2001).
11. M. Morys, F. M. Mims III, S. Hagerup, S. E. Anderson, A. Baker, J. Kia, and T. Walkup, "Design, calibration, and performance of MICROTOPS II handheld ozone monitor and sun photometer," J. Geophys. Res. **106,** 14,573–14,582 (2001).
12. P.-Y. Deschamps, B. Fougnie, P. Lecomte, and C. Verwaerde, "SIMBAD: a field radiometer for satellite ocean-color validation," Appl. Opt. **43,** 4055–4069 (2004).
13. M. R. Reynolds, M. A. Miller, and M. J. Bartholomew, "A fast-rotating, spectral shadowband radiometer for marine applications," J. Atmos. Ocean. Tech. **18,** 200–214 (2001).
14. M. A. Miller, M. J. Bartholomew, and R. M. Reynolds, "The accuracy of marine shadow-band measurements of aerosol optical thickness and Ångström exponent," J. Atmos. Ocean. Tech. **21,** 397–410 (2004).
15. K. M. Markowitz, P. J. Flatau, P. K. Quinn, C. M. Carrico, M. K. Flatau, A. M. Vogelmann, D. Bates, M. Liu, and M. Rood, "Influence of relative humidity on aerosol radiative forcing: an ACE-Asia experiment perspective," J. Geophys. Res. **108,** 8662–8673 (2003).
16. R. R. Draxler, "Hybrid sigle-particle Lagrangian integrated trajectories (HY-SPLIT): Version 3.0," Users Guide and Model Description, Tech. Rep. ERL ARL-195 (National Oceanic and Atmospheric Administration, Silver Spring, MD., 1992).
17. K. D. Knobelspiesse, C. Pietras, G. S. Fargion, M. Wang, R. Frouin, M. A. Miller, A. Subramaniam, and W. M. Balch, "Maritime aerosol optical properties measured by handheld sun photometers," Remote Sens. Environ. **93,** 87–106 (2004).
18. C. Pietras and G. S. Fargion, "Sun-pointing-error correction for sea deployment of the MICROTOPS II handheld sun photometer," J. Atmos. Ocean. Tech. **20,** 767–771 (2003).
19. G. Thuillier, M. Hersé, D. Labs, T. Foujols, W. Peetermans, D. Gillotay, P. C. Simon, and H. Mandel, "The solar spectral irradiance from 200 to 2400 nm as measured by the SOLSPEC spectrometer from the ATLAS 1-2-3 and EURECA missions," Solar Phys. **214,** 1–22 (2003).
20. B. N. Holben, T. F. Eck, I. Slutsker, N. D. Tanre, J. P. Buis, A. Setzer, E. Vermote, J. A. Reagan, Y. Kaufman, T. Nakajima, F. Lavenu, I. Jankowiak, and A. Smirnov, "AERONET—a federated instrument network and data archive for aerosol characterization," Rem. Sens. Environ. **66,** 1–16 (1998).
21. C. N. Long, D. L. Slater, and T. Tooman, "Total sky imager model 880 status and testing results," U.S. Department of Energy Atmospheric Radiation Measurement Program Tech. Rep. TR-006 (U.S. Government Printing Office, 2001), p. 36.
22. A. Ignatov, "Sensitivity and information content of aerosol retrievals from AVHRR: radiometric factors," Appl. Opt. **46,** 991–1011 (2002).
23. N. T. O'Neill, A. Ignatov, B. Holben, and T. Eck, "The log-normal distribution as a reference for reporting aerosol optical depth statistics; empirical tests using multi-year, multi-site AERONET sun photometer data," Geophys. Res. Lett. **27,** 3333–3336 (2000).
24. A. Ignatov and L. Stowe, "Aerosol retrievals from individual AVHRR channels. II. Quality control, probability distribution functions, information content, and consistency checks of retrievals," J. Atmos. Sci. **59,** 335–362 (2001).
25. G. Fargion, R. Barnes, and C. McClain, "*In Situ* aerosol optical thickness collected by the SIMBIOS program (1997–2000): Protocols, and data QC and analysis," NASA Tech. Memo. 2001-209982 (NASA Goddard Space Flight Center, Greenbelt, Md., 2001), pp. 11–21.